In: 2023 AIAA Aviation and Aeronautics Forum and Exposition (AIAA AVIATION Forum), San Diego, 12-16 June 2023
AIAA 2023-3309; DOI:10.2514/6.2023-3309

Aerodynamics of a Compact Nacelle at Take-Off Conditions

Avery Swarthout, David MacManus, Fernando Tejero, Jesús Matesanz-García
Ioannis Goulos, Luca Boscagli[1]
Centre for Propulsion and Thermal Power Engineering, Cranfield University

Christopher Sheaf[2]
Rolls Royce Plc, Derby

Next generation ultra-high bypass ratio turbofans may have larger fan diameters than the previous generation of aircraft engines. This will potentially increase the nacelle diameter and may incur penalties to the weight and drag of the powerplant. To offset these penalties, a more compact nacelle may be used. Compact nacelles may be more sensitive to boundary layer separation at the end-of-runway conditions, particularly at an off-design windmilling operating point. Additionally, the flow separation on the external cowl surface is likely to be influenced by the integration between the powerplant, pylon and airframe. The publicly available NASA high lift common research model (HL-CRM) with take-off flap and slat settings was modified to accommodate an ultra-high bypass ratio powerplant. The powerplant has an intake, separate jet exhaust, external cowl and pylon. Boundary layer separation on the external cowl of the compact powerplant is assessed at end-of-runway rated take-off and take-off windmilling scenarios. Additionally, the lift curve and C_p distributions of the high lift common research model (HL-CRM) are compared for rated take-off and take-off windmilling engine mass flows. Overall, the nacelle boundary layer separates from the nacelle highlight at windmilling conditions when the engine mass flow is relatively low. The mechanism of separation at windmilling conditions is diffusion driven and is initiated on the nacelle aft-body. The pylon has a small impact on the overall mechanism of separation. However, the wing and high-lift devices of the HL-CRM introduce local separation on the external cowl. The HL-CRM wing with the installed powerplant stalls at a similar angle ($\alpha_{a/c}$ = 16°) to the HL-CRM with the through flow nacelle available in the open literature. Compared with the nominal take-off condition, the maximum lift coefficient of the HL-CRM airframe was reduced by about 2% under windmilling engine mass flows.

Nomenclature

C	=	Wing Chord (m)
C_L	=	Lift Coefficient
C_p	=	Pressure Coefficient
D_{cruise}	=	Cruise Drag (N)
$D_{diversion}$	=	Diversion Drag (N)
$D_{inc.Mach}$	=	Increased Mach Drag (N)
dx	=	Horizontal Installation Position (m)
dz	=	Vertical Installation Position (m)
k_1	=	Downselection Coefficient 1
k_2	=	Downselection Coefficient 2
l_{fore}	=	Forebody Length (m)
l_{nac}	=	Nacelle Length (m)
l_{sep}	=	Separation Length (m)
M	=	Free Stream Mach Number
M_{ise}	=	Isentropic Mach Number

[1] Centre for Propulsion and Thermal Power Engineering, Cranfield University
[2] Installation Aerodynamics Specialist, Installation Aerodynamics, Rolls Royce Plc.

MFCR = Mass Flow Capture Ratio
Re_{MAC} = Aircraft Reynolds Number based on Aircraft Mean Aerodynamic Chord
r_{fan} = Fan Radius (m)
r_{hi} = Highlight Radius (m)
r_{if} = Leading Edge Initial Radius of Curvature (m)
r_{te} = Trailing Edge Radius (m)
V_x = Streamwise flow velocity (m/s)
V_z = Vertical flow velocity (m/s)

$\alpha_{nac,\ isol}$ = Isolated/Free Flying Nacelle Angle of Attack (degrees)
$\alpha_{nac,\ inst}$ = Installed Nacelle Angle of Attack (degrees)
$\alpha_{nac,\ crit}$ = Nacelle Critical Angle of Attack (degrees)
$\alpha_{a/c}$ = Aircraft Angle of Attack (degrees)
β_{nac} = Boat Tail Angle (degrees)
φ = Azimuthal Position (degrees)
φ_{pitch} = Powerplant Installed Pitch Angle (degrees)
φ_{toe} = Powerplant Installed Toe Angle (degrees)
γ = Upwash Angle (degrees)
γ_{ref} = Reference Upwash Angle (degrees)

I. Introduction

Ultra-high bypass ratio (UHBR) turbofans can reduce the fuel consumption of next generation aircraft by increasing propulsive efficiency [1]. The maximum bypass ratio of a modern in-service engine is around 12 and UHBRs are expected to have bypass ratios above 15 [2]. This may result in a larger fan and by extension, a larger nacelle. To offset the weight and drag penalties incurred by larger nacelles, a more compact, short nacelle may be used. However, compact nacelles may be more sensitive to boundary layer separation at operating conditions such as end of runway (EoR) [3]. Additionally, these compact nacelles may be more prone to boundary layer separation at off-design, take-off windmilling conditions where the engine mass flow capture ratio (MFCR) is reduced relative to the design conditions. As MFCR is reduced there is an increase in spillage around the nacelle lip [4]. Significant acceleration of the flow around the highlight introduces high peak Mach numbers at the nacelle leading edge. Downstream, there is possibility of a diffusion led boundary layer separation over the nacelle aft body [3]. In addition, the potential interaction between the nacelle, pylon and wing may affect the mechanism of separation on the nacelle [5], [6]. Boundary layer separation on both the powerplant and airframe may arise due the high incidence and low MFCR under windmilling conditions as well as interactions between the high-lift devices, pylon, nacelle, and airframe. This work investigates the characteristics of boundary later separation for installed, compact nacelles at both rated take-off and take-off windmilling mass flow conditions at the end of runway.

A. Common Research Model High-Lift Aerodynamics

The NASA common research model (CRM) is representative of a widebody, long range commercial aircraft [7]. Lacy and Sclafani established a high lift version of this aircraft that incorporates the flaps, slats, their respective fairings, and a through-flow nacelle with inboard chine [8]. It has two configurations, one for landing and one for take-off (Table 1). This is referred to as the high lift CRM (HL-CRM). A 10% semispan wind tunnel model of the HL-CRM was developed for CFD validation [9]. Evans et al. [10] published experimental results for the lift and drag polars of the semi-span model at both take-off and landing conditions. Results were compared with those obtained from the NASA 14x22 foot wind tunnel to establish a framework for quantifying experimental uncertainty for high lift aerodynamics. These tests established a set of reference data against which numerical models of the HL-CRM can be compared. To date, CFD efforts to quantify the HL-CRM maximum lift coefficient have mainly focused on the landing configuration [5], [6]. One of the original HL-CRM publications by Lacy and Sclafani describes the flap and slat positioning at landing and take-off. RANS calculated lift and drag polars are provided for both configurations [8]. Flow topologies at post stall conditions are presented for the main wing suction surface. Aside from this, detailed computational investigations of boundary layer separation for high lift aircraft configurations has mostly been limited to the landing version of the aircraft [11], [12], [13], [14]. Furthermore, details of the powerplant aerodynamics are largely neglected[13]. One reason for this is that the HL-CRM has been typically investigated with a through-flow nacelle [14], [15]. This does not facilitate application of the typical exhaust pressure ratios or mass flow capture ratios associated with windmilling or take-off conditions. The novelty of this work is in the assessment of a representative

long-range UHBR powerplant installed on the HL-CRM with take-off flap and slat settings. This includes analysis of the impact of the pylon, high lift devices, and airframe on the nacelle boundary layer separation onset and mechanism at both windmilling (MFCR < 0.550) and maximum take-off (MFCR ~ 1.500) conditions.

Flap and Slat Angle Settings for HL-CRM

Configuration	Inboard Slat	Outboard Slat	Inboard Flap	Outboard Flap
Landing	30°	30°	37°*	37°*
Take-Off	22°	22°	25°**	25°**

*Split Flap **Sealed Flap

Table 1: The flap and slat angle settings used on each of the HL-CRM configurations.

B. Nacelle Design and Selection Process

In previous work a compact nacelle (l_{nac}/r_{hi} = 3.1) was designed in isolation using a multi-point, multi objective CFD-in-the-loop optimizer [3]. The optimisation considered both on-design cruise and off-design windmilling conditions [3]. Thresholds were applied on the windmilling objectives to limit the boundary layer separation at those conditions. The nacelle geometry is symmetric along the X-Z plane and the 3D geometry is controlled with 5 aero-lines equally spaced along the half azimuth (Figure 1) [16], [17]. Each aeroline is parameterized with 4 constrained parameters and 4 degrees of freedom that are used to define an intuitive class shape transformation (iCST) curve [18]. The bulk dimensions of the nacelle such as length (l_{nac}), highlight radius (r_{hi}), trailing edge radius (r_{te}), scarf and droop were held constant. The degrees of freedom for each aeroline are forebody length (l_{fore}), maximum radius (r_{max}), initial radius of leading-edge curvature (r_{if}) and boat-tail angle (β_{nac}). With 5 total aerolines, this yields a 20 degree of freedom optimisation problem (Figure 1). Optimisation convergence was assessed through a hypervolume index [18]. Starting from a Latin hypercube sampling (LHS) of 400 individuals for the initial design space exploration, the optimisation applied a CFD-in-the-loop approach with subsequent generations of 150 individuals. When the change in hypervolume between 2 generations was less than 0.01, the optimisation was converged. This occurred after 16 generations, including the LHS. A nacelle candidate was selected from the converged, non-dominated Pareto of the optimisation for use in this analysis. The candidate selected from the Pareto front had the minimum mid cruise drag (D_{cruise}) provided that its sensitivity to drag rise at increased Mach number and diversion windmilling conditions were within specified thresholds. For the selected candidate nacelle, $D_{inc.mach}$ (M = 0.87) < $k_1 D_{cruise}$ (M = 0.85) and $D_{diversion}$ (M = 0.65) < $k_2 D_{cruise}$ (M = 0.85). k_1 and k_2 are design choice coefficients [4].

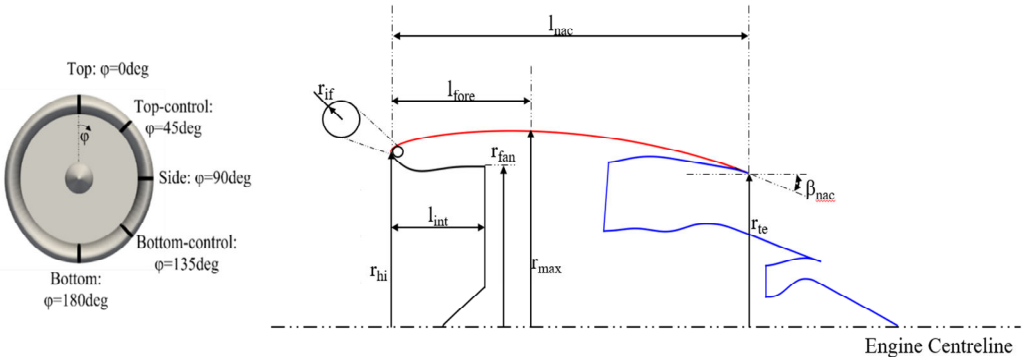

Figure 1: Placement of the individual aerolines around the nacelle azimuth (left) and the intuitive parameters used to define each aeroline iCST (right).

C. Scope of the Present Work

This work describes the impact of the pylon and airframe on flow separation onset for compact nacelles at the end of runway (M_{inf} = 0.25, α_{nac} ~ 20° [19]) conditions. Additionally, the impact of a windmilling engine, with very low mass

flow, on the aircraft lift distribution is assessed at the end of runway condition. In this work, the term powerplant refers to the combination of a nacelle, intake, and separate jet exhaust configuration. A method is used to assess the relative contributions of the pylon and airframe on the critical incidence of the nacelle and the boundary layer separation mechanism. The nacelle critical incidence is considered as the incidence at which boundary layer separation on the nacelle top line ($\varphi = 0°$) starts at the highlight. Two operating conditions are studied (Table 2). Of primary interest is the off-design windmilling condition, where boundary layer separation is most likely to arise. The impact of windmilling on the aircraft and powerplant performance are investigated. At this windmilling condition, the exhaust pressure ratios and temperatures are matched to free stream static conditions. The MFCR is below 0.55. To evaluate the impact of MFCR on the flow separation onset, a second, nominal take-off condition is studied for comparison (maximum take-off). At this condition, the MFCR is more than 3 times greater than for the windmilling case. Additionally, the exhaust pressure ratios and temperatures were obtained from a representative engine performance model.

II. Methodology

A. Powerplant Airframe Integration Methodology

The isolated powerplant comprises nacelle, intake, and separate jet exhaust (Figure 2(a)). To isolate the impact of the pylon on nacelle boundary layer separation, a free flying configuration is defined (Figure 2(b)). The free flying powerplant is installed on the HL-CRM modified with take-off flap and slat settings (Figure 2(c)). In this way, a hierarchical approach is implemented to study the engine-airframe installation effects. This allows the aspects of powerplant airframe integration that contribute to flow separation under high lift conditions to be identified. The HL-CRM used in this body of work neglects the high lift fairings and chine. Based on the approach from the NASA drag prediction workshop 6 (DPW6) [7], the powerplant was positioned at a spanwise location of 37.5% of the total wingspan. Pitch and toe angles of 1.75° and 2.25° are applied to the nacelle and pylon on the wing, based on the throughflow nacelle from DPW6 [7]. In order to place the candidate nacelle in a similar position to the HL-CRM through-flow nacelle [6], a Z-axis offset from the wing leading edge of dz/C=0.15 was chosen (Figure 2). The nacelle trailing edge at $\varphi = 0°$ was positioned to be coincident with the wing leading edge along the streamwise axis (dx/C = 0.0). The axial coincident position, (dx/C = 0.0) is selected as a trade-off between installation benefits at mid-cruise conditions (M = 0.85, MFCR ~ 0.700) and potential installation positions for a UHBR turbofan [20].

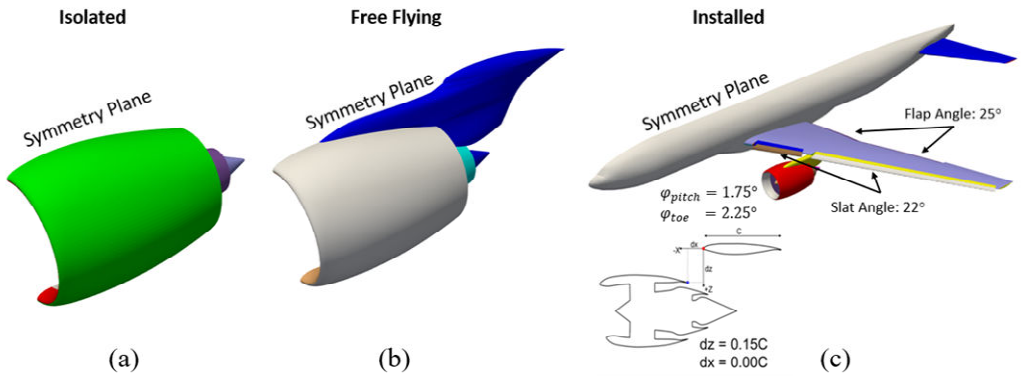

Figure 2: Description of the installation types investigated within this study and the parameters which describe the installation of the powerplant on the HL-CRM.

D. Operating Conditions

Each configuration was assessed across a range of increasing incidence to establish the point of boundary layer separation onset and development. The mass flow capture ratio (MFCR) of a UHBR powerplant at maximum take-off conditions is approximately 1.50 - 1.70 [21], [22]. In this work, the MFCR of the powerplant at rated maximum take-off conditions is taken as 1.50. During windmilling at the end-of-runway, the mass flow capture ratio will be below 0.55 [4]. The isolated, free flying and installed configurations were each assessed at a low MFCR consistent with windmilling (MFCR < 0.55) and at a MFCR consistent with maximum take-off (MTO) (MFCR ~ 1.50) (Table 2).

Conditions Assessed for End of Runway Aerodynamics

Installation Type	Condition	Mach Number	MFCR	Nacelle Incidence (α_{nac})(degrees)
Isolated	Windmilling	0.25	< 0.55	14-30
	Maximum Take-Off	0.25	~ 1.50	14-30
Free Flying	Windmilling	0.25	< 0.55	10-20
	Maximum Take-Off	0.25	~ 1.50	10-20
Installed	Windmilling	0.25	< 0.55	14-30
	Maximum Take-Off	0.25	~ 1.50	14-30

Table 2: The operating conditions assessed for each type of installation.

The operating conditions at take-off are characterized by low Mach number and high incidence. The maximum nacelle incidence when installed on the aircraft ($\alpha_{nac,\,inst}$) associated with the take-off can be up to 20° [19]. Additionally, the lift coefficient of the HL-CRM at take-off conditions may be in the range of 1.8-2.0 [10], [11]. This means that a significant amount of upwash is generated ahead of the wing which increases the local incidence onto the installed nacelle. For the computational models of the isolated and free flying configurations, the nacelle incidence ($\alpha_{nac,isol}$) is prescribed as a far field boundary condition. When installed on an aircraft, the aircraft angle of attack is prescribed as a boundary condition. The total incidence for the installed nacelle ($\alpha_{nac,inst}$) is then estimated as the sum of the following three components: aircraft angle of attack ($\alpha_{a/c}$), installed pitch angle (φ_{pitch}) and the estimated reference upwash angle (γ_{ref}) (Figure 3). In this way, the isolated, free flying and installed nacelles can be compared at a broadly similar incidence ($\alpha_{nac,isol} \approx \alpha_{nac,inst}$) although it is acknowledged that this is a simplification.

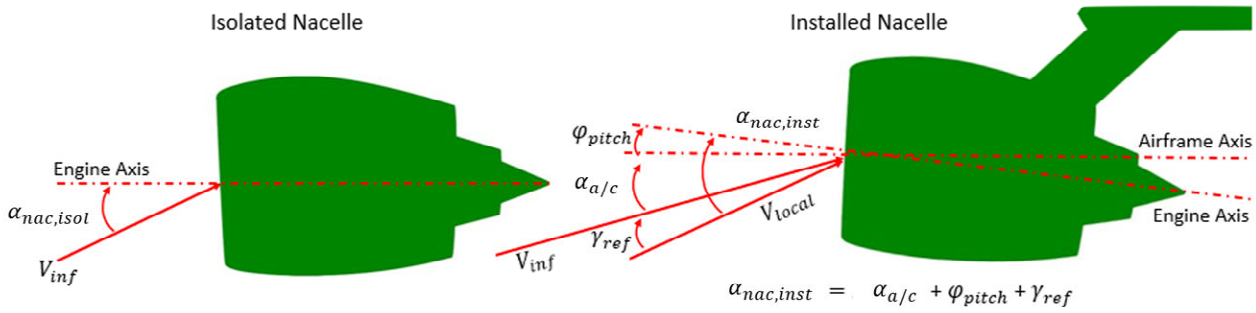

Figure 3: The nomenclature used to define α_{nac} for isolated nacelles (left) compared against the nomenclature for installed nacelles (right).

When installed on the HL-CRM, the candidate nacelle has a pitch angle relative to the airframe central axis of φ_{pitch} =1.75° (Figure 2). Aerodynamic upwash also increases the effective incidence onto the nacelle. The upwash angle is calculated using the following equation:

$$\gamma = \arcsin\left(\frac{V_z}{\sqrt{V_x^2 + V_z^2}}\right) - \alpha_{a/c} - \varphi_{pitch}$$

Where V_x is the velocity parallel to the streamwise axis and V_z is the velocity normal to the streamwise axis. The reference upwash angle (γ_{ref}) along the nacelle centreline plane at a reference location 1.0 l_{nac} upstream of the nacelle leading edge [23].

E. CFD methodology

The meshes for the isolated, free flying and installed cases are comprised of unstructured tetrahedra with prism layers in the near wall regions. The first cell height near the wall corresponds to a target y^+ under 1 to resolve the boundary layer without wall functions. To achieve this, the isolated nacelle requires 49 million elements, the free flying nacelle has approximately 58 million elements and the installed nacelle case with the HL-CRM has about 260 million elements. The external cowl and intake mesh sizing been validated based on work by Tejero et al. [18]. The methodology for the CFD and meshing for the exhaust and pylon has been validated against the Dual Separate Flow Reference Nozzle (DSFRN) by Goulos et al. [20] and Hueso-Rebassa [24].

For the HL-CRM, guidance in the mesh sizing has been derived from the 4th High Lift Prediction Workshop [6]. Matesanz et al performed a mesh sensitivity study that compared the meshing approach used within this study against a coarser mesh of approximately 89 million elements [25]. The aircraft C_L was reduced by 0.006% between the coarse mesh (89 million elements) and fine mesh (260 million elements). However, the airframe drag was more sensitive to changes in the mesh size, therefore the fine mesh was adopted for this work.

The CFD solutions were obtained using the steady, implicit, pressure-based Favre Averaged Navier Stokes (RANS) equations [26]. The kω-SST turbulence model is used for all the calculations. The Green-Gauss Node Based Gradient scheme was used to get gradients of the flow variables such as temperature and pressure. The momentum and turbulence terms were solved with a nominal 2nd order upwind discretization scheme.

III. Results and Discussion

A. Maximum Take-Off Conditions (M = 0.25, MFCR ~ 1.50)

At Maximum Take-Off (MTO) conditions, the mass flow capture ratio is approximately 1.50 and there is no flow spillage over the external cowl. The peak surface Mach number for the isolated nacelle cowl does not exceed 0.36 at the maximum incidence assessed in the study (α_{ref}) (Figure 4(d)). Across the range of incidence assessed (Table 2), there is no discernable separation of the boundary layer for the isolated nacelle (Figure 4(a)-(d)).

As the nacelle incidence is increased from α_{nac} = 14° - 29°, the peak isentropic Mach number over the cowl highlight increases from 0.25 to 0.36. At the trailing edge, surface Mach number reduces from 0.25 to about 0.22 across the same range of incidence. Therefore, magnitude of the streamwise adverse pressure gradient is increasing. Additionally, the surface streaklines begin to diverge at the trailing edge of the cowl under the influence of a spanwise pressure gradient. For α_{nac} = 29°, the surface Mach number at the top aeroline trailing edge (φ = 0°) is about 0.02 higher than for φ = 30°. This indicates that when the boundary layer does separate at these conditions (M = 0.25, MFCR ~ 1.50), it will be from the top aeroline (φ = 0°) trailing edge.

Similarly, although the pylon has an impact on the local flow field for the free flying nacelle, there is no discernable separation at any of the incidences assessed within this study at maximum take-off conditions (M = 0.25, MFCR ~ 1.50) (Figure 4(a)-(d)). The peak isentropic Mach number at the nacelle highlight is about 0.02 lower for the free flying nacelle when compared against the isolated nacelle at the same incidence. Overall, the pylon has a small impact on the sensitivity of the external cowl to boundary layer separation at these conditions.

For the installed configuration, at the typical take-off conditions (M = 0.25, MFCR ~ 1.50), The boundary layer on the outboard nacelle surface remains attached across the range of incidence (Figure 4(a)-(d)). However, on the nacelle inboard surface, there is a local separation around the pylon/nacelle corner (Figure 4(a)-(d)). This separation is present across the entire range of incidences considered for the HL-CRM at maximum take-off conditions (M = 0.25, MFCR ~1.50). At $\alpha_{a/c}$ =10°, the inboard surface separation is initiated at around $0.6l_{nac}$ (Figure 4(a)) and extends to the trailing edge. When $\alpha_{a/c}$ is increased to 17°, the separation grows upstream slightly and is initiated at around $0.5l_{nac}$ (Figure 4(d)).

Previous literature reported that the $\alpha_{a/c}$ at which HL-CRM main wing stalls to be about 16° for the take-off configuration with flap and slat deflection angles of 25° and 22° respectively (Table 1) [8], [12]. The operating conditions used within this work are somewhat different from those applied in previous literature. The take-off conditions for the full-scale HL-CRM reported by Lacy and Sclafani are at sea level ISA conditions [8]. The free stream Mach number in that work is 0.2 [8]. Within this work, the maximum take-off conditions are at 15,000 ft above mean sea level and free stream Mach number of 0.25. In terms of the Reynolds number based on the aircraft mean

aerodynamic chord (Re_{MAC}), the HL-CRM with through flow nacelle at take-off was $Re_{MAC} \sim 33x10^6$ [8]. The HL-CRM with representative powerplant at the take-off conditions within this work has $Re_{MAC} \sim 27x10^6$.

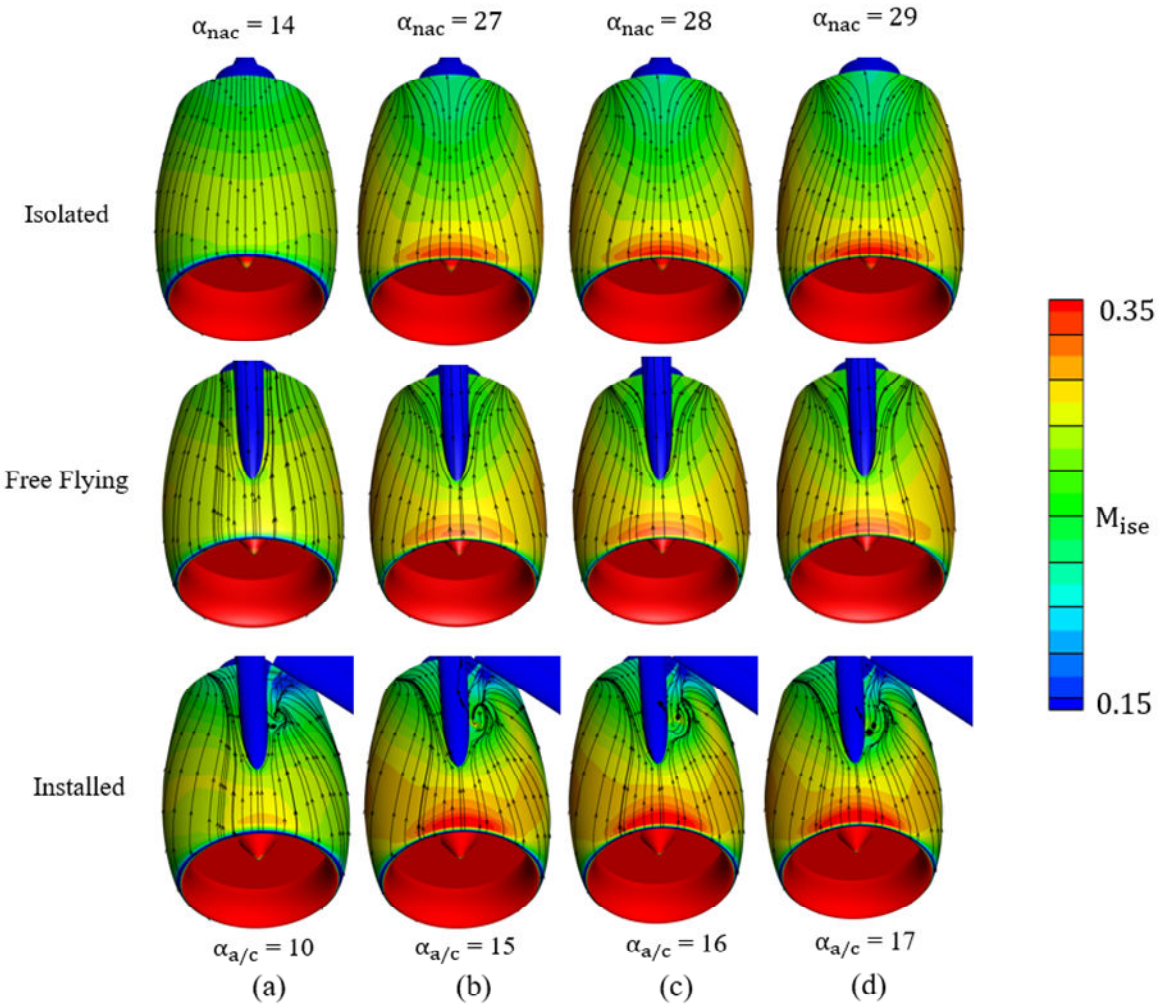

Figure 4: Effect of α_{nac} on nacelle surface M_{ise} distribution and streaklines for the isolated, free flying and installed nacelles at take-off conditions (M = 0.25, MFCR ~ 1.50).

B. Windmilling Conditions (M = 0.25, MFCR < 0.55)

In this work, the nacelle critical incidence, α_{crit}, is considered as the point at which boundary layer separation starts from the highlight. When this happens, the boundary layer does not reattach downstream. For the isolated nacelle at windmilling conditions (MFCR < 0.55), boundary layer separation starts at $\alpha_{nac,isol} = 27°$ (Figure 5). The separation is initiated on the aft-body of the external cowl directly at the top aeroline ($\varphi = 0°$) (Figure 6(b)). The streamwise length of this separation grows from $0.02l_{nac}$ to $0.4l_{nac}$ as the incidence increases from 27° to 28° (Figure 6(b)-(c)). For $\alpha_{nac,isol} = 28°$, the leading point of the separated region coincides approximately with the nacelle crest (Figure 6(c), Figure 5). After a subsequent increase to $\alpha_{nac,isol} = 29°$, the separated region extends from the leading edge to the trailing edge (Figure 5, Figure 6(d)). Azimuthally, the separated region extends approximately ±22.5° around the nacelle and is centered on the top line ($\varphi = 0°$). It has been previously shown that the aft-body, diffusion induced separation mechanism at windmilling is largely independent of the individual nacelle design and design method [3].

The critical incidence (α_{crit}) of the free flying cowl is 28°, 1 degree lower than for the isolated cowl (Figure 5). When α_{nac} is 2 degrees lower than α_{crit}, local separation is present in the corner between the nacelle cowl and pylon (Figure 6(b)-(c)). As the incidence is increased from 26° to 27°, 1 degree below α_{crit}, this locally separated region grows from the nacelle aft-body up to the nacelle crest (Figure 6(b)-(c)). As the incidence is increased by another 1 degree to α_{crit} (29°), the nacelle forebody boundary layer at $\varphi = 0°$ is separated from the highlight to the trailing edge (Figure 6(d)). This is broadly similar to the isolated case even though there are some differences due to the presence of the pylon for the free flying nacelle. With incorporation of the pylon, $\alpha_{nac,crit}$ is 28°compared with 29° for the isolated nacelle (Figure 5). Compared with the isolated nacelle, the length and azimuthal extent of the separated flow region are broadly similar.

For the combined airframe and powerplant at the end of runway windmilling condition (M= 0.25, MFCR < 0.55), separation develops in the junctions between the nacelle and pylon at an aircraft incidence of $\alpha_{a/c} = 10°$ (Figure 6(a)). An $\alpha_{a/c} = 10°$ approximately corresponds to an $\alpha_{nac,\,inst} = 14°$ when the pitch angle and reference upwash are considered. For $\alpha_{a/c} = 10°$, this separation starts at around $0.4l_{nac}$ at the inboard side and further aft at $0.5l_{nac}$ on the outboard side (Figure 6(a)). These local separations around the pylon extend to the trailing edge of the nacelle. On the inboard side of the nacelle, there is a notable crossflow due to the installation and impact of the high-lift system which affects the flow around the pylon. For both the inboard and outboard nacelle surfaces at windmilling MFCR > 0.55, the extent of the separation regions around the nacelle/pylon interface grows gradually as $\alpha_{a/c}$ increases. At $\alpha_{a/c} = 16°$, the two separated regions each extend from the trailing edge up to the pylon leading edge (Figure 6(c)). At this angle-of-attack, a separation node is present on the cowl inboard surface, directly downstream of the highlight. This shows the top of the cowl forebody is close to complete flow separation. As $\alpha_{a/c}$ increases from 16° to 17°, the separation moves upstream and starts from the nacelle highlight (Figure 6(a)-(d)). Taking into account $\alpha_{a/c}$ (17°), the aerodynamic upwash angle (Υ_{ref} ~2.80°), and installation pitch angle (φ_{pitch} ~ 1.75°) the equivalent nacelle incidence for which the separation starts from the highlight is approximately $\alpha_{nac,inst} \approx 23°$ (Figure 5).

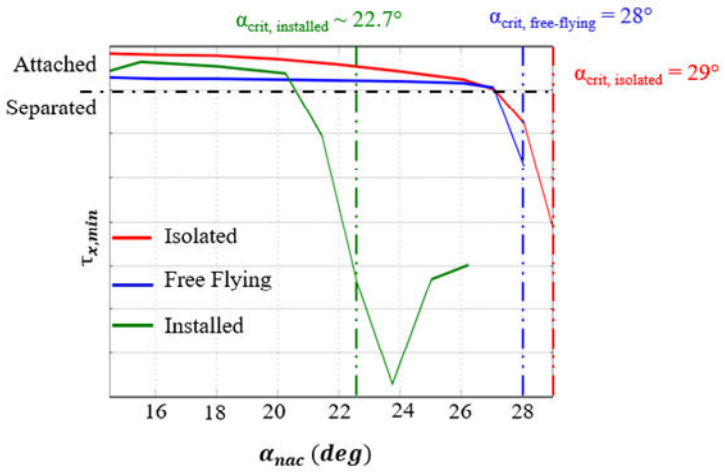

Figure 5: Variation of minimum wall shear stress ($\tau_{x,min}$) with nacelle incidence (α_{nac}) at end of runway windmilling conditions (M = 0.25, MFCR < 0.55) for the isolated, free flying and installed nacelle.

Overall, boundary layer separation on the cowl forebody at high incidence is driven by the low mass flow capture ratio at windmilling (M = 0.25, MFCR < 0.55). At maximum take-off conditions (M = 0.25, MFCR ~ 1.50), separation did not appear on either the isolated or free flying nacelle over the range of incidence (Figure 4). When the nacelle was installed on the HL-CRM, the local separation that forms on the inboard nacelle surface arises independently of the MFCR. It is present at both maximum take-off (M = 0.25, MFCR ~ 1.50) and windmilling conditions (M = 0.25, MFCR < 0.550) (Figure 4, Figure 6). This local separation on the inboard cowl results from an interaction between the nacelle, wing, and high-lift devices. Although not considered within the present study, a chine would typically be incorporated in order to mitigate the interaction between the nacelle, pylon, wing and high lift devices, which can affect boundary separation on the aircraft main wing [13]. However, separation on the outboard nacelle surface did not arise under maximum take-off conditions (M = 0.25, MFCR ~ 1.5). It only appeared under influence of the low MFCR associated with windmilling conditions (M = 0.25, MFCR < 0.55). Therefore, the mechanism of the diffusion

led separation which then extends from the nacelle leading edge at windmilling is relatively unaffected by the pylon and HL-CRM airframe. In this assessment, steady RANS calculations are used, and the unsteadiness of the separated flows is neglected. With such large regions of boundary layer separation, the flow field will be unsteady which is an areas of expected future investigations.

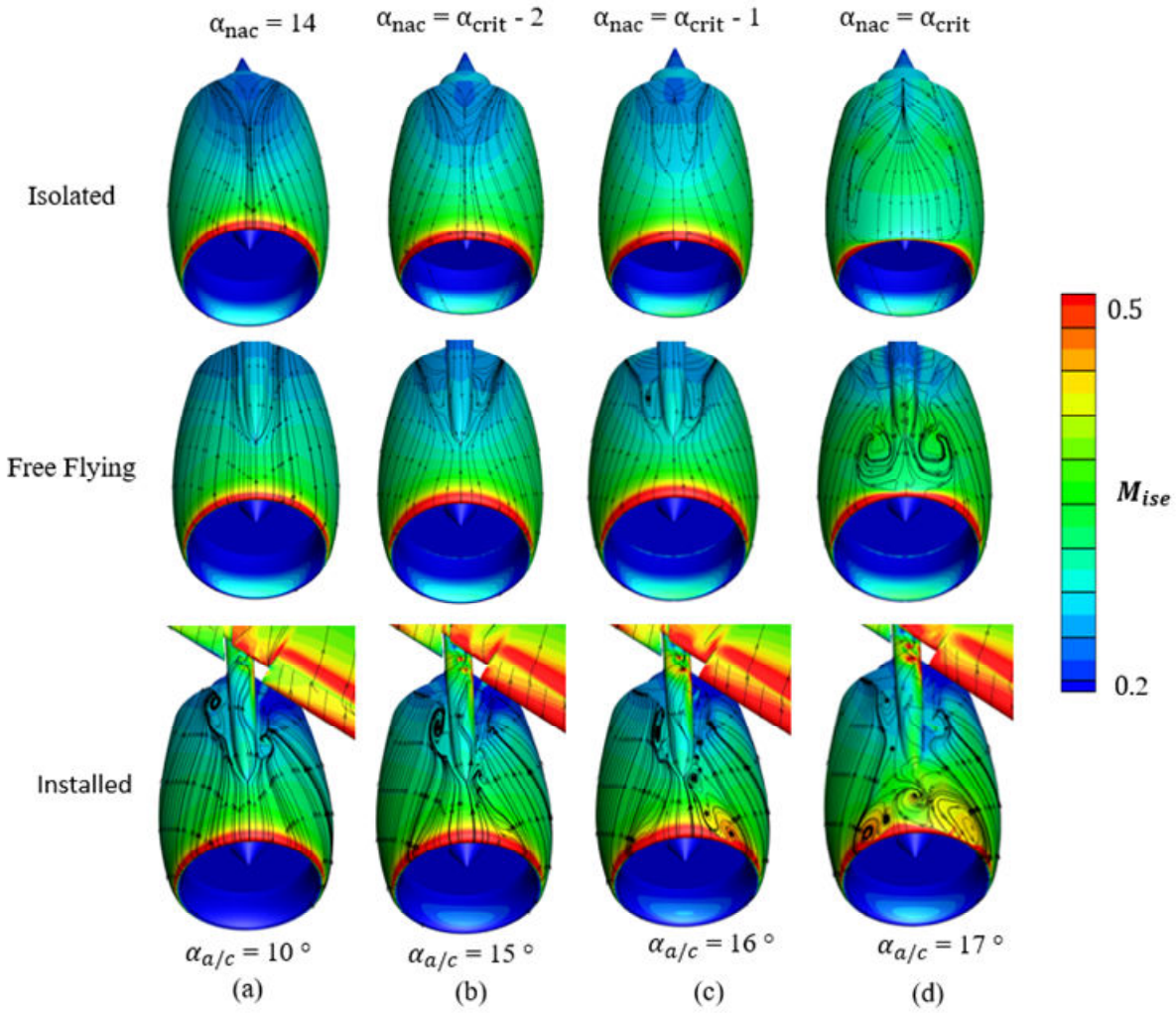

Figure 6: Effect of α_{nac} on Mise distribution and surface streaklines for the installed nacelle configuration at end of runway windmilling (M = 0.25, MFCR < 0.55).

C. Impact of Windmilling Conditions on Aircraft Aerodynamics

In the following assessment, only the pressure and viscous terms acting on the surfaces of the HL-CRM airframe are accounted for in the calculation of the airframe lift coefficient (C_L) i.e., the powerplant and pylon are not included. Additionally, the HL-CRM is assessed with a symmetry plane (Figure 2). Therefore, the lift coefficients reported are for one half of the HL-CRM airframe. During windmilling, it is envisioned that one engine is operating at the low windmilling massflow while the other remains functional. Due to the symmetry plane in the CFD, only the windmilling powerplant is represented for this case (M = 0.25, MFCR < 0.55).

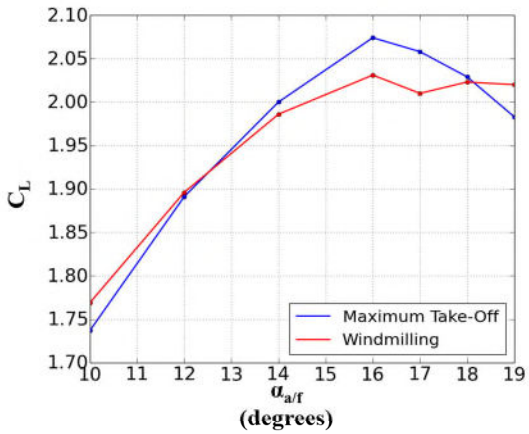

Figure 7: Variation of lift coefficient (C_L) with $\alpha_{a/c}$ for the half HL-CRM with nacelle at take-off (M = 0.25, MFCR ~ 1.500) and windmilling conditions (M = 0.25, MFCR < 0.550).

Previous literature with both experiments and CFD have reported the incidence for which the HL-CRM main wing stalls ($\alpha_{a/c,\ crit}$) as 16° [8], [10], [11]. The version of the HL-CRM presented in the other literature has a through-flow nacelle that is smaller than the nacelle in this study. The through-flow nacelle also lacks the separate jet exhaust employed on the powerplant here. With the separate jet exhaust, the effect of representative engine mass flows, exhaust pressures and temperatures can be assessed. Despite these differences, the main wing for the HL-CRM with the installed, representative powerplant is also predicted to lose lift at 16° (Figure 7). The maximum C_L reported for the HL-CRM with the through flow nacelle at take-off (Re_{MAC} ~ $33x10^6$) is reported as between 2 and 2.1 [8]. The maximum C_L of the HL-CRM with the representative powerplant at maximum take-off conditions is calculated to be 2.07 (Re_{MAC} ~ $27x10^6$). This is similar to the previous computational work on the HL-CRM with the through flow nacelle, despite the modest differences in Reynolds number. At both maximum take-off (M = 0.25, MFCR ~ 1.500) and windmilling (M = 0.25, MFCR < 0.55) conditions, the lift increases monotonically with incidence up to $\alpha_{a/c}$ = 16° (Figure 7). The difference in MFCR and exhaust pressure ratios between the maximum take-off and windmilling conditions has some impact on the airframe lift coefficient across the range of $\alpha_{a/c}$ assessed. For $\alpha_{a/c}$ = 10°, the HL-CRM at windmilling (M = 0.25, MFCR < 0.55) has a C_L that is 0.02 greater than for the maximum take-off case (M = 0.25, MFCR ~ 1.50) (Figure 7). Up to around $\alpha_{a/c}$ = 12°, the C_L for the HL-CRM at windmilling (M = 0.25, MFCR < 0.550) is greater than for the maximum take-off case (M = 0.25, MFCR ~ 1.500) (Figure 7). From $\alpha_{a/c}$ = 14° to $\alpha_{a/c}$ = 16°, it is expected that the HL-CRM will be close to stall [8]. For these angles of attack, the C_L for the HL-CRM at maximum take-off conditions exceeds that at windmilling. At $\alpha_{a/c}$ = 14° the difference in C_L is about 0.015. This difference rises to about 0.04 for $\alpha_{a/c}$ = 16° (Figure 7). This difference in C_L at $\alpha_{a/c}$ = 16° is approximately 2% of the maximum airframe C_L at take-off conditions (M = 0.25, MFCR ~ 1.50).

For the HL-CRM with the powerplant at windmilling conditions (M = 0.25, MFCR < 0.550) relative to maximum take-off conditions (M = 0.25, MFCR ~1.50), there are differences in the wing pressure side C_p distribution that reflect the differences in MFCR and nozzle pressure ratios between the two operating conditions considered. These differences arise in the region of wing that is outboard of the pylon, as well as between the pylon and wing root (Figure 8). They contribute to the difference in airframe C_L (Figure 7).

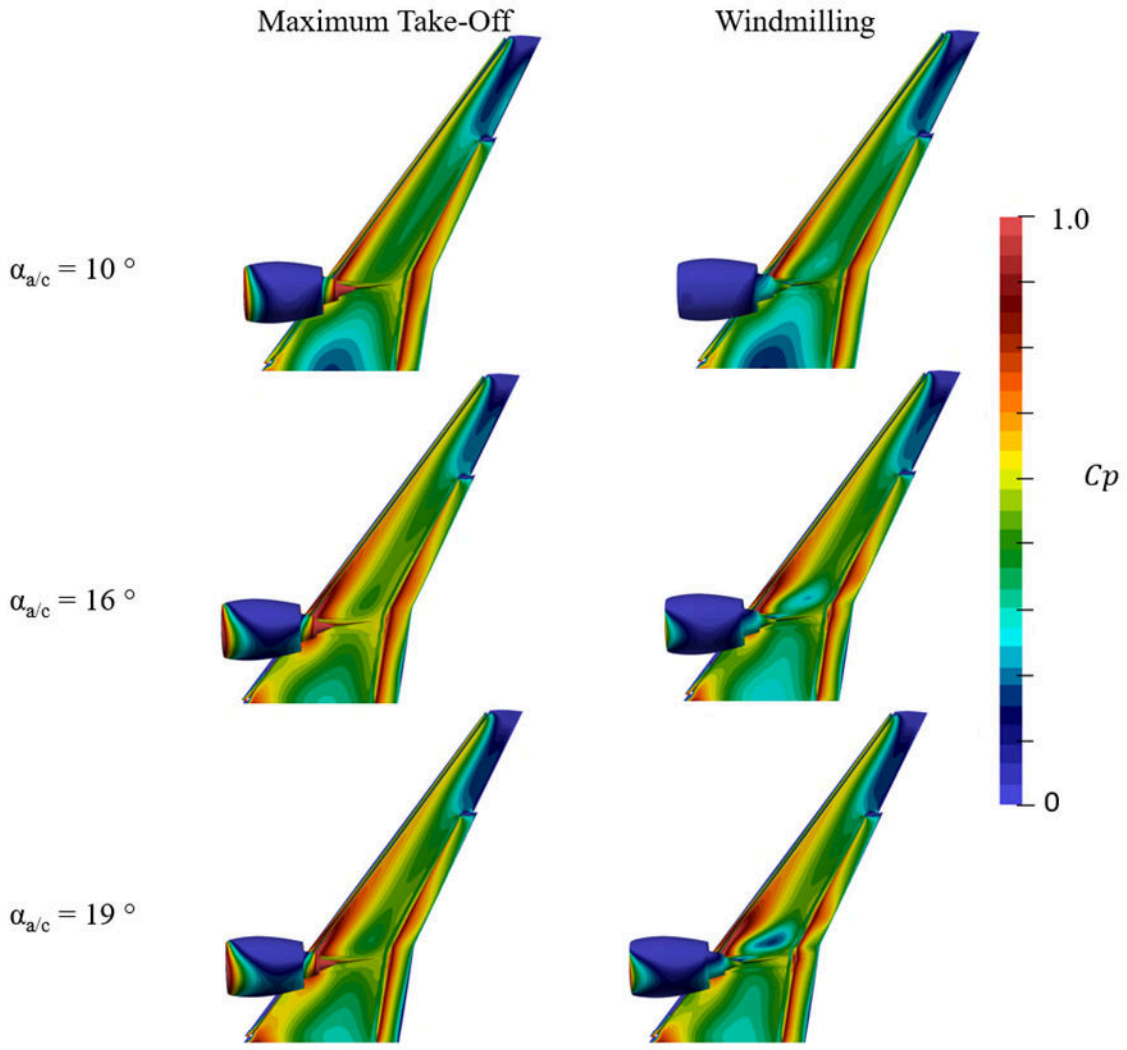

Figure 8: Variation of HL-CRM lower wing surface pressure coefficient with $\alpha_{a/c}$ for both the maximum take-off (M = 0.25, MFCR ~ 1.500) and windmilling (M = 0.25, MFCR < 0.550) cases.

At $\alpha_{a/c}$ = 10°, outboard of the pylon and on the wing pressure side, the C_p is around 0.15 higher for the maximum take-off case (M = 0.25, MFCR ~ 1.500) relative to the windmilling case (M = 0.25, MFCR < 0.550) (Figure 8). The differences in the C_p distribution between the maximum take-off (M = 0.25, MFCR ~ 1.50) and windmilling case (M = 0.25, MFCR < 0.55) becomes more pronounced as the incidence is increased to $\alpha_{a/c}$ = 16-19°. For $\alpha_{a/c}$ = 16°, the difference in wing pressure side C_p outboard of the pylon grows to around 0.35 (Figure 8). As the MFCR is reduced from 1.5 to 0.55, a region of reduced C_p close to the wing root grows in size (Figure 8). Overall, windmilling (M = 0.25, MFCR < 0.55) leads to penalizing regions of reduced C_p on the lower surface of the wing around the pylon and wing root relative to maximum take-off conditions (M = 0.25, MFCR ~ 1.50).

On the HL-CRM wing suction surface, the differences in pressure distribution between the windmilling and maximum take-off cases are less pronounced compared with the wing pressure side. For $\alpha_{a/c}$ = 10°, there is a slightly higher C_p on the aft end of the wing root for the maximum take-off (M = 0.25, MFCR ~ 1.50) case compared with the windmilling case (M = 0.25, MFCR < 0.55) (Figure 9). For $\alpha_{a/c}$ = 16-19°, there are some differences in the topology of the C_p on the wing section that is aft of the pylon and nacelle (Figure 9). However, this is within the HL-CRM post-stall regime, where the flows are likely to be separated as has been reported in previous literature about the HL-CRM [11], [14], [15]. Overall, the low MFCR at windmilling has a minor impact on the pressure distribution on the main wing suction side, even for $\alpha_{a/c}$ = 16-19° where the nacelle forebody flow is separated for the windmilling case (M = 0.25, MFCR < 0.55) but not for the maximum take-off case (M = 0.25, MFCR ~ 1.50).

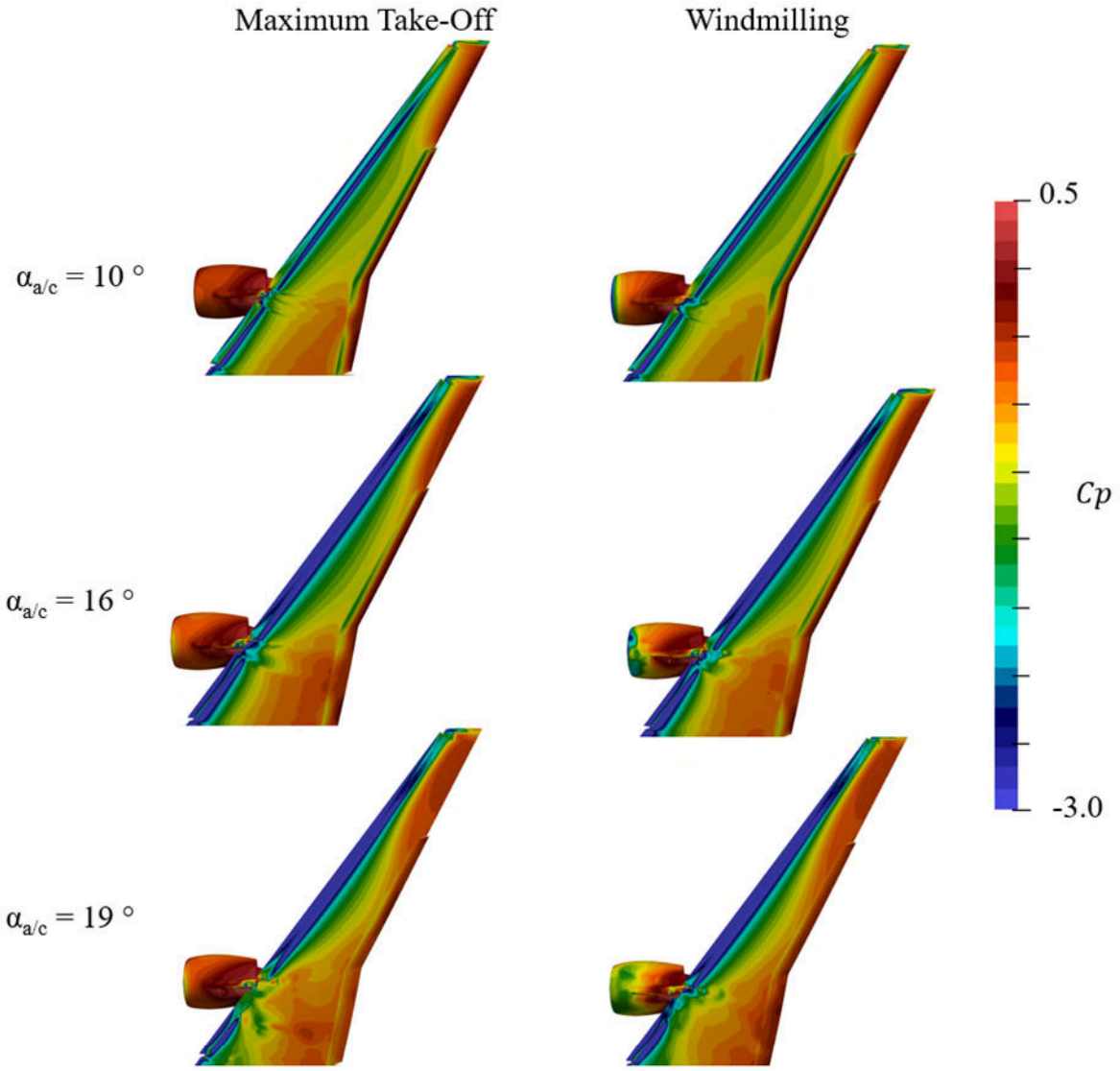

Figure 9: Variation of HL-CRM wing suction pressure coefficient with $\alpha_{a/c}$ for both the windmilling (M = 0.25, MFCR < 0.550) and maximum take-off (M = 0.25, MFCR ~ 1.50) cases.

IV.Conclusion

This work presents the analysis of a powerplant with a compact nacelle at the end of runway conditions associated with maximum take-off (M = 0.25, MFCR ~ 1.50) and windmilling (M = 0.25, MFCR < 0.55) conditions. The nacelle is analysed in three different ways for each condition: isolated, free flying, and installed configurations. The compact nacelle was optimized within a previous work using a multi-point, multi-objective framework that accounts for both rated take-off and take-off windmilling conditions [3]. At maximum take-off conditions (M = 0.25, MFCR ~ 1.50), with high engine mass flows, separation is not present on either the isolated or free flying nacelle external cowl at any incidence investigated. When installed on the HL-CRM, a local separation arises on the nacelle inboard side. This separation results from an interaction between the nacelle, wing and high lift devices.

At end of runway windmilling conditions, with a relatively low engine mass flow, flow separation is initiated by a subsonic diffusive mechanism on the nacelle aft body. Separation for the isolated nacelle starts at a $\alpha_{nac,isol} = 27°$ and grows with further increase in $\alpha_{nac,isol}$ up to 29°. The isolated nacelle is then fully separated from the leading edge. Installation of the nacelle on the HL-CRM airframe introduces regions of local flow separation at lower incidences

but does not modify the overall mechanism of separation from the highlight. On the inboard nacelle surface there is a corner separation resulting from an interaction between the nacelle, pylon and high lift devices. This separation manifests independently of mass flow capture ratio. The separated region on the outboard nacelle surface arises directly due to the low MFCR (< 0.55) during windmilling conditions. This separation grows as $\alpha_{a/c}$ increases. In the approach to stall, boundary layer separation occurs over the entire nacelle upper surface for the windmilling case (MFCR < 0.55) which does not arise at the higher take-off MFCR ~ 1.50. Despite the differences in flow separation topology at lower incidence between the isolated and installed nacelles, they both undergo a complete boundary layer separation from the nacelle leading edge to trailing edge. This is a direct result of the low MFCR < 0.55 due to the windmilling conditions. While windmilling does not affect the incidence for which the maximum lift coefficient arises on the HL-CRM, it reduced the lift coefficient at $\alpha_{a/c} = 16°$ by about 2% relative to a maximum take-off condition (M = 0.25, MFCR ~ 1.50).

V. Acknowledgements

This project has received funding from the Clean Sky 2 Joint Undertaking (JU) under grant agreement number 101007598. The JU receives support from the European Union's Horizon 2020 research and innovation programme and the Clean Sky 2 JU members other than the Union.s

VI. References

[1] Daggett, D. Ultra-Efficient Engine Technology Systems Integration and Environmental Assessment. NASA Tech. Rep. CR-2002-211754, 2002.

[2] Birch, N. "2020 Vision: The Prospects for Large Civil Aircraft Propulsion," The Aeronautical Journal, vol. 104, no. 1038, pp. 347–352, 2000, doi: 10.2514/1.C033040

[3] Swarthout, A., MacManus, D., Tejero, F., Matesanz-García, J., Boscagli, L., and Sheaf, C. "A comparative assessment of multi-objective optimisation methodologies for aero-engine nacelles," ICAS 2022-0162. ICAS 33rd Technical Congress, September 2022.

[4] Schreiner, B., Tejero, F., MacManus, D., and Sheaf, C. "Robust Aerodynamic Design of Nacelles for Future Civil Aero-Engines." Proceedings of the ASME Turbo Expo 2020: Turbomachinery Technical Conference and Exposition, Volume 1: Aircraft Engine; Fans and Blowers. Virtual, Online. September 21–25, 2020. V001T01A015.

[5] Rumsey, C. "1st High Lift Prediction Workshop," Hiliftpw.larc.nasa.gov, Available: https://hiliftpw.larc.nasa.gov/index-workshop1.html.

[6] Rumsey, C. "4th High Lift Prediction Workshop," Hiliftpw.larc.nasa.gov, Available: https://hiliftpw.larc.nasa.gov/.

[7] Tinoco, E., Brodersen, O., Keye, S., Laflin, K., Feltrop, E., Vassberg, J., Mani, M., Rider, B., Wahls, R., Morrison, J., Hue, D., Roy, C., Mavriplis, D., and Murayama, M. "Summary Data from the Sixth AIAA CFD Drag Prediction Workshop: CRM Cases," Journal of Aircraft, vol. 55, no. 4, pp. 1352-1379, 2018.

[8] Lacy, D., and Sclafani, A. "Development of the High Lift Common Research Model (HL-CRM): A Representative High Lift Configuration for Transonic Transports," AIAA Paper 2016-0308. 54th AIAA Aerospace Sciences Meeting, January 2016.

[9] Lin, J., Pack Melton, L., Viken, S., Andino, M., Koklu, M., Hannon, J., and Vatsa, V. "High Lift Common Research Model for Wind Tunnel Testing: An Active Flow Control Perspective," AIAA 2017-0319. 55th AIAA Aerospace Sciences Meeting, January 2017.

[10] Evans, A., Lacy, D., Smith, I., and Rivers, M. "Test Summary of the NASA High-Lift Common Research Model Half-Span at QinetiQ 5-Metre Pressurized Low-Speed Wind Tunnel," AIAA Paper 2020-2770. AIAA Aviation 2020 Forum, June 2020.

[11] Vatsa, V., Lin, J., Melton, L., Lockard, D., and Ferris, R., "CFD Simulations of Landing and Takeoff CRM High-Lift Configurations," AIAA Paper 2021-2499. AIAA Aviation 2021 Forum, August 2021.

[12] Lacy, D., and Clark A., "Definition of Initial Landing and Takeoff Reference Configurations for the High Lift Common Research Model (CRM-HL)," AIAA Paper 2020-2771. AIAA Aviation 2020 Forum, June 2020.

[13] Koklu M., Lin J., Hannon J., Melton L., Andino M., Paschal K., and Vatsa V., "Investigation of the Nacelle/Pylon Vortex System on the High-Lift Common Research Model," AIAA Journal, vol. 59, no. 9, pp. 3748-3763, 2021.
[14] Ghate A., Stich G., Kenway G., Housman J., and Kiris C., "A Wall-Modeled LES Perspective for the High Lift Common Research Model Using LAVA," AIAA Paper 2022-3434. AIAA Aviation 2022 Forum, June 2022.
[15] Vatsa V., Lin J., Melton, L., Lockard, D., and Ferris, R., "CFD Simulations of Landing and Takeoff CRM High-Lift Configurations," AIAA Paper 2021-2499. AIAA Aviation 2021 Forum, August 2021.
[16] Tejero, F., MacManus, D., Sanchez-Moreno, F., and Sheaf C., "Neural network-based multi-point, multi-objective optimisation for transonic applications", Aerospace Science and Technology, vol. 136, no. 108208, 2023
[17] Tejero, F., MacManus, D., and Sheaf, C., "Surrogate-based aerodynamic optimisation of compact nacelle aero-engines," Aerospace Science and Technology, vol. 93, no. 105207, 2019.
[18] Tejero, F., MacManus, D., Matesanz García, J., Swarthout, A. and Sheaf, C., "Towards the design and optimisation of future compact aero-engines: intake/fancowl trade-off investigation", International Journal of Numerical Methods for Heat & Fluid Flow, 2022, doi: 10.1108/HFF-06-2022-0366
[19] Hoelmer, W., Younghans, J., & Raynal, J. Effect of Reynolds number on upper cowl flow separation. Journal of Aircraft, vol. 24, no. 3, pp. 161-169. 1987, doi: 10.2514/3.45411
[20] Goulos, I., Otter, J., Tejero, F., Hueso-Rebassa, J., MacManus, D., and Sheaf, C."Civil turbofan propulsion aerodynamics: Thrust-drag accounting and impact of engine installation position," Aerospace Science and Technology, vol. 111, p. 106533, 2021.
[21] Peters, A., "Ultra Short Nacelles for Low Fan Pressure Ratio Propulsors," PhD Thesis, Massachusetts Institute of Technology, 2014
[22] Silva, V., Lundbladh, A., Petit, O., Xisto, C., "Multipoint Aerodynamic design of Ultrashort Nacelles for Ultra High Bypass Ratio Engines" Journal of Propulsion and Power, vol. 38, no. 4, pp. 541-558, 2022
[23] Crawford, T., Dobosy, R., & Dumas, E., "Aircraft wind measurement considering lift-induced upwash. Boundary-Layer Meteorology," vol. 80. no. 1-2, pp. 79-94, 1987, doi: 10.1007/BF00119012
[24] Hueso-Rebassa, J., "Design, Performance and Aerodynamics of Non-Axisymmetric Exhaust Systems for Civil Aero-Engines," PhD thesis, Cranfield University, 2022
[25] Matesanz-Garcia, J., MacManus, D., Tejero, F., Goulous, I., Hueso Rebassa, J., Swarthout, A., Christie, R., "Coupled propulsive and aerodynamic analysis of an installed ultra-high bypass ratio nacelle; comparison between end-of-runway, start-of-climb, and cruise conditions", presented at AIAA Aviation Forum 2023, June 2023.
[26] ANSYS, Inc. (2018). ANSYS Fluent User's Guide, Release 19.1.

2023-06-08

Aerodynamics of a compact nacelle at take-off conditions

Swarthout, Avery E.

IEEE

Swarthout A, MacManus D, Tejero F, et al., (2023) Aerodynamics of a compact nacelle at take-off conditions. In: 2023 AIAA Aviation and Aeronautics Forum and Exposition (AIAA AVIATION Forum), 12-16 June 2023, San Diego, USA. Paper number AIAA 2023-3309
https://doi.org/10.2514/6.2023-3309